Kinetic studies of hydrothermal carbonization of avocado stone and analysis of the polycyclic aromatic hydrocarbon contents in the hydrochars produced

Diakaridia Sangare, Agnes Chartier, Mario Moscosa-Santillan, Iskender Gökalp, Stéphane Bostyn

Kinetic Studies of Hydrothermal Carbonization of Avocado Stone and Analysis of the Polycyclic Aromatic Hydrocarbon Contents in the Hydrochars Produced.

Diakaridia Sangare[1,2], Agnes Chartier[4], Mario Moscosa-Santillan[1], Iskender Gökalp[2], Stéphane Bostyn[2,3,*]

[1] Facultad de Ciencias Químicas Universidad Autónoma de San Luis Potosí Av. Dr. Nava # 6, Zona Universitaria San Luis Potosí, S.L.P., CP: 78210, México

[2] Institut de Combustion, Aérothermique, Réactivité, et Environnement (ICARE)-CNRS UPR3021, 1C avenue de la recherche scientifique 45071 Orléans Cedex 2, France

[3] Université d'Orléans, Institut Universitaire de Technologie, 16 rue d'Issoudun BP16724 45067 Orléans Cedex 2, France

[4]Institut de Chimie Organique et Analytique (ICOA), Université d'Orléans-CNRS, 8 Rue de Chartres BP 6759, 45067 Orléans cedex 2, France

* Correspondence: Email: stephane.bostyn@univ-orleans.fr; Tel: +33238255476; Fax: +33238696004.

Abstract:

Model-free and model-fitting kinetic approaches were used to investigate the hydrothermal carbonization (HTC) of avocado stone. The total solid mass yield was used to estimate the kinetic parameters and reaction mechanism. The results obtained show that the HTC process for avocado stones could be divided into four temperature zones. Up to 160 °C, the initial induction period where the reaction rate is relatively slow. The second zone (160 to 200 °C) corresponds to the maximum decomposition rate. The third zone between 200 and 220 °C corresponds to the stabilization zone; in this zone, the total solids yield is practically constant, and finally, the polymerization zone, between 220 and 250 °C, where an increase in total solid yield was observed. The kinetic parameters and reaction mechanism were determined in two temperature zones, from 150 to 210 ºC and 210 to 250 ºC. In the first zone, the decomposition of avocado stone during the HTC process followed a random nucleation reaction mechanism (Avrami-Erofeev-1) with the activation energy of 87.84 ± 3.28 kJ/mol. In contrast, in the second zone, it followed a first-order reaction model, and the activation energy was 230.96 ± 28.84 kJ/mol. Analysis of PAHs with gas chromatography-mass spectrometry showed that the number of PAHs in the hydrochar increases with an increase in temperature from 190 to 250 ºC. The 3-4 rings

PAHs were dominant in the hydrochars prepared at temperatures between 230 and 250 ºC, while two rings were largely prevalent in the hydrochar obtained at low temperatures.

Keywords: Avocado stone; hydrothermal carbonization; Kinetic model; PAHs

1 INTRODUCTION

The increasing demand for energy and the rapid depletion of fossil fuels are the reasons for the need to find new sources of energy, sustainable technologies, or processes that are environmentally friendly. This problem has inspired researchers to study and develop more efficient and reliable tools to exploit biomass as a source of renewable energy. The thermochemical conversion processes of biomass have better industrial prospects for biomass valorization since the process conditions can be optimized to maximize gas, liquid, and solid yields [1]. Among thermochemical processes, hydrothermal carbonization (HTC) of biomasses (agro-industrial, forestry, and urban waste) has received widespread attention in recent years because of its efficiency and convenience [2, 3]. HTC technology is based on a thermochemical conversion process by which it converts organic material into carbonized material (hydrochar), liquid (bio-oil mixed with water), and small fractions of gases. The HTC process is performed in the temperature range of 180-250°C, during which biomass is submerged in water and is heated under autogenous saturated vapor pressure between 10 and 40 bars and residence time ranging from a few minutes up to several hours [4]Under these process conditions, water exhibits a behavior similar to that of an organic solvent owing to changes in its polarity and dielectric constant and acts as a catalyst for the conversion of biomass through hydrolysis, dehydration, decarboxylation, aromatization, condensation, and polymerization [5]. Through the HTC process, researchers have investigated distinct types of biomass, tomato waste [6], sugarcane bagasse [7], olive pomace [4], corn cob [8], and olive stones [9]. Most of these biomasses are agro-industrial wastes. Avocado stones is some of the most massive agro-industrial wastes generated in Mexico.

The avocado is one of the most frequently consumed fruits in the world. Mexico is globally the leading avocado producing country, with more than 45% (~2.18 million tons/year) of the total production in 2020 [10]. Products derived from avocados include ice cream, drinks, and

guacamole being the most marketed product [11]. There are also examples of avocado oil production, which is of a quality similar to olive oil [12]. Avocado processing generates an enormous amount of waste, particularly the skin and seed or stone. The stone represents 15.0–16.0% of the fruit weight [13]. A significant amount (~170,000 tons/year) of avocado production is guacamole, and this represents more than 25,000 tons of waste per year [14].

The technology of the HTC process of waste to form hydrochar and bio-oil has been is the focus in recent years [6, 8, 9]. During the HTC process, hydrochar formation can be carried out in two reaction pathways. The formation can proceed from the reaction of the solid-solid pathway known as primary hydrochar (P-HC), in which hydrochar maintains the original structural elements and morphology of the parent biomass matrix; and the hydrochar formation can be carried out from aqueous phase degradation of the biomass followed by polymerization of the organic molecules into a solid phase, called secondary hydrochar (S-HC). This secondary hydrochar is extractable with organic solvents [15]. This S-HC is a sequential result of hydrolysis, dehydration, and isomerization during HTC to produce furfurals and their derivatives. The furfurans and their derivatives polymerize as microspheres, these microspheres can be further carbonized by dehydration reactions, resulting in an amorphous solid that is soluble in organic solvents [15]. Although, Paksung et al.[16] reported that it is not easy to distinguish analytically between P-HC and S-HC; because both appear as a single solid mass of char.

The main product of HTC is hydrochar, a solid material 55-74% rich in carbon, is the stable, a lignite-like material which is characterized by a high heating value (21.1–30.6 MJ/kg) [4] and its physical, chemical, and mechanical properties make it susceptible to different uses. Hydrochar can thus be used directly as a solid fuel that can be burned for energy or produce syngas. Most recently, the hydrochar has also been applied as an additive agent for soil amendment [17, 18]. The hydrochar has proved to be a favorable soil of amendment, increased cation extraction capacity, and reduced solid bulk density [19]. However, for the soil use of hydrochars, contaminants such as heavy metals and polycyclic aromatic hydrocarbons (PAHs), in hydrochars are of significant concerns.

Peng et al. [17] reported a significant increase of PAHs in the hydrochar of municipal solid waste, with the increase in temperature of HTC between 160°C and 240°C. The formation of

PAHs from biomass is -a multi-step process. The S-HC formation during the hydrothermal carbonization of biomass leads to increased PAHs formation and their retention in the primary hydrochar [20, 21].

Biomass decomposition by HTC is dominated by chemical reactions similar to pyrolysis; however, the HTC process is initiated by hydrolysis, leading to biomass decomposition temperatures lower than those of pyrolysis [23]. The HTC reaction mechanisms complexity has led some authors to develop lumped kinetics models to describe it [24]. For simplification, the authors have used the biomass components model, such as cellulose, hemicellulose, and lignin. For example, Reza et al. [25]determined the activation energy of cellulose and hemicellulose in the temperature range between 200 and 260°C. They reported that cellulose degradation is described by a first-order rate constant with an activation energy 73±6 kJ/mol, and hemicellulose degradation has an activation energy of 30±12 kJ/mol. For the same operating conditions (200-260°C), Killer et al. [26] reported activation energy values equal to 61 kJ/mol and 127 kJ/mol for hemicellulose and cellulose, respectively. On the other hand, Liu and Balasubramanian [27] considered the HTC process as a first-order reaction and estimated the activation energy for coconut fibers (67.5 kJ/mol) and eucalyptus leaves (59.2 kJ/mol). Recently Pecchi et al.[28] reported Ea values of 139.16 and 161.68 kJ/mol and reaction orders of about 2.68 and 2.46, for digestate and sludge, respectively, using Differential Scanning Calorimetry. As can be seen, different approaches have been used to determine the kinetic parameters during the HTC process of the biomass. However, researchers have used conventional methods in only a few studies to determine kinetic parameters. Methods based on thermal analysis, such as thermogravimetric analysis, have been widely used in the literature to study biomass decomposition kinetics. They are high-precision methods that can be used for the quantitative examination of processes as well as for estimating useful kinetic parameters for various thermal decomposition reactions. Since thermogravimetric analysis is a technique based on mass loss or conversion as a function of temperature and time during thermochemical conversion, a similar analogy can be used for the HTC process based on the hydrochar mass yield as a function of temperature and reaction time.

For this reason, this research - focuses on the determination of the kinetic parameters that described the hydrothermal carbonization process of the avocado stone, using the thermal analysis technique in an open-loop controller system. The biomass's HTC behavior was studied using the total solid mass yield or hydrochar yield produced at different temperatures and times.

The kinetic predictions were made by using the Model-Free Method, such as FWO, KAS, and Friedman and the Model-Fitting Methods were used to determine the most appropriate kinetic model mechanism of HTC reactions. In addition, a qualitative analysis of the hydrochars produced was performed to determine the structure of polycyclic aromatic hydrocarbons (PAHs).

2 MATERIALS AND METHODS

2.1 Feedstock

In this study, avocado stones (AS) of the *Hass* variety from Michoacán (Mexico) were used. In general, an AS has a moisture content between 65 and 75% [29], which is ideal for HTC. Initially, an AS was cut and dried in a stove at 80 °C for storage; subsequently, it was ground to obtain a particle size between 0.5 and 1mm. **Table 1** contains the physical and chemical characteristics associated with the raw AS. The details of the determination of these parameters were explained in our previous study [30].

Table 1. Proximate, ultimate, extractive, hemicellulose, cellulose, lignin analysis, and higher heating value characteristics of AS

Proximate analysis (%)	
MC	3.2±0.4
VM	72.5±1.7
FC [a]	22.4±1.0
Ash	1.9±0.6
Ultimate analysis (%)	
Carbon	46.1±0.2
Hydrogen	6.4±0.1
Nitrogen	0.02 ± 0.0
Sulphur	nd
Oxygen [a]	47.9±0.9
Extractives (%)	3.6±0.4
Hemicellulose (%)	76.4±0.3
Cellulose [a] (%)	3.0±0.3
Lignin (%)	17.0±0.3
HHV(MJ/kg)	18.6±0.2
MC: moisture content; VM: volatile matter; FC: fixed carbon; nd: not detected; [a]:by difference	

2.2 HTC Reactor Description and Experimental Procedure

The detailed descriptions of the experimental procedures can be found in our previous studies [31]. Briefly, the HTC experiments were carried out in the stirred autoclave reactor (Top Industrie, France) with an internal volume of 300 mL suitable for a pressure of 100 bars. This stirred autoclave reactor consisted of a reactor vessel and a cylindrical capping vessel. The

capping vessel included a central connection for a magnetic stirrer (max. 1500rpm, 50 W) and connections for measuring pressure, monitoring temperatures, and releasing the gases. For each HTC run,18.65 ± 0.05 g of dry sample were loaded into the reactor together with 186.5 ± 1.5 g of deionized water, with a biomass-to-water ratio (AS/W) equal to 1/10 (w/w). Before starting the heating program, the residual air inside the reactor was removed using a vacuum pump to a pressure of less than 40 mbar. The reactor was heated from room temperature to setpoint temperature at different powers supplied in the reactor 160, 200, and 240 W; these represent overall average heating rate of 1.5, 2.0, and 2.8 °C/min, respectively. The setpoint temperature was varied from 150 °C to 250 °C. For powers of 160 and 240 W, the setpoint temperatures were 150, 170, 190, 210, 230 and 250 ºC, while for power of 200 W the setpoint temperatures were 150 to 250 ºC with a 10 ºC increase. The setpoint temperatures of 150, 190, and 250 ºC were carried out in triplicate; allowing to define an error less than 1.5% in all cases. During the experiment, the reactor was stirred at 550 rpm. After the reactor reaches the setpoint temperature, it was immediately cooled down, and this took 5 to 10 minutes to cool it down by immersing it in a 5 °C water bath. After cooling the reactor, the system pressure was noted, the reactor was opened, the liquid and solids were separated with a Whatman filter paper with a pore size of 11 microns, and the solid was weighed after drying at 105 °C for 24 hours in the stove. The hydrochar yield or total solid yield (Y_{HC}) was determined through the **Eq.(1)**:

$$Y_{HC} = \frac{m_{HC}}{m_{bio}}.100 \quad (1)$$

Where m_{HC} is the mass of total solid (on a dry base), and m_{bio} is the raw biomass mass (on a dry base). The derivative hydrochar yield (DY_{HC}) is the first-order derivative of Y_{HC} with respect to time. From this approach, it is possible to determine the maximum temperature decomposition of biomass. The DY_{HC} was determined through the **Eq.(2)**:

$$DY_{HC} = \frac{\Delta Y_{HC}}{\Delta t} \quad (2)$$

Where DY_{HC} is derivative hydrochar yield (%/min), ΔY_{HC} is the difference between Y_{HC} from one setpoint temperature to another, and Δt is the time variation (min) between setpoint temperatures.

2.3 HTC reactor heat-up and reaction time

In reality, the constant temperature during HTC is not correct in batch autoclave reactors because there are different step of heating: i) a heating time, ii) a holding time temperature, and finally,

iii) a cooling time. In many publications in the literature, the definition of reaction time is not standardized. Often, HTC reaction time starts to be counted when the set HTC temperature is reached [4] while in some other cases [32] includes heat-up time. The heat-up time may be neglected only if it is very rapid as it could be the case when the HTC is performed in batch micro-reactors. In this study, an open-loop system was used, where the power supplied to the furnace of the reactor is controlled (i.e., constant in each experiment), and we consider the reaction time of the HTC is the heat-up time until the setpoint temperature is reached.

Fig. 1 shows the different heating time profiles established for different setpoint temperatures at 200 W electrical power (**Fig. 1a**) and for the different electrical powers used (**Fig. 1b**). In this case, holding time temperature and cooling time was not considered because when the setpoint temperature was reached, the reactor was cold down from setpoint temperature to room temperature; it took 5 to10 minutes to cool it down by immersing it in a 5°C water bath.

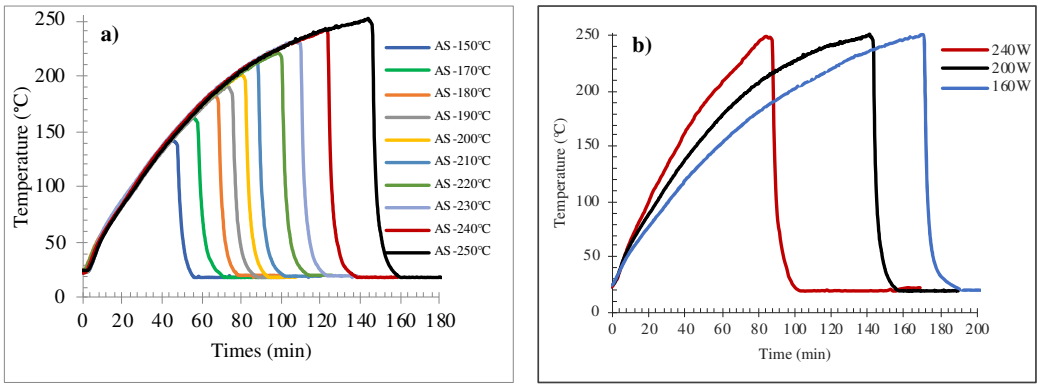

Fig. 1: Temperature trends vs. time of hydrothermal tests, **(a)** conducted at 200W to set-point temperature, (**b**) different powers (heating rate) from ambient temperature to 250 °C.

2.4 Secondary hydrochar extraction and GC–MS analyzer

Extraction of S-HC was performed with toluene (100%) as the extraction solvent in a Soxhlet extractor. Toluene is a good solvent for the extraction of tar, such as PAHs, in hydrochar [33].

For each extraction, about 2 g of hydrochar and 250 mL toluene were placed in the Soxhlet extractor for 36 h. After this time, the solution was concentrated by a rotary evaporator to obtain 25 mL volume. The S-HC composition was detected using a GC–MS analyzer. The analysis was carried out by two different methods and columns to detect aliphatic and PAHs compounds.

Aliphatic compounds were detected on a Trace Ultra-ISQ gas chromatograph single quadrupole mass spectrometer (Thermo Scientific, Villebon Sur Yvette, France) equipped with a

programmed temperature vaporizing injector (PTV) and a 2 mm diameter. Thermo PTV liner was used. A DB35ms column (30 m length, 0.25 mm internal diameter, and 0.25 μm film thickness) was installed in the GC oven. Initially the temperature of the GC oven was set at 80 °C for 2 min followed by a 10 °C/min ramp to 200 °C and a 15 °C/min ramp to 320 °C with a 5 min hold. For the data acquisition using the Electron Impact (EI) mode, the transfer line temperature and the ion source were held at 315 °C and 250 °C, respectively. A mass range (m/z 50–300 amu with a dwell time of 0.2s) was scanned in full scan acquisition. In order to detect PAHs, the extracted liquid was diluted 50 times in dichloromethane. The PAHs were detected on a Trace Ultra gas chromatography coupled with a quadrupole mass spectrometer. A DB17ms Agilent column (30 m length, 0.32 mm internal diameter, and 0.25 μm film thickness) was installed in the GC oven. Initially, the temperature of the GC oven was set at 40 °C for 7 min followed by a 20 °C/min ramp to 75 °C, and it was held on for 15 minutes and then a 20 °C/min ramp to 200 °C for 8 minutes, and finally a 10 °C/min ramp to 220 °C, and it was held on for 55 minutes. For the data acquisition using the Electron Impact (EI) mode, both the temperature of the transfer line and the ion source was held at 200 °C. The temperature for the inlet injector was fixed at 300 °C for attaining a well-vaporization of the sample, and a spitless liner was installed. A mass range (m/z) of 50–300 amu was scanned, that is, in full scan acquisition.

2.5 Kinetic models and mechanisms of the HTC process of biomass

A model is a theoretical and mathematical description of what occurs experimentally. This study will analyze the kinetic models that can describe the kinetic reaction of the HTC process of the biomass, based only on the formation of hydrochar (evolution of the solid phase). The overall reaction of the biomass in the HTC process is presented in the following reaction:

$$\text{Biomass} + H_2O \rightarrow \text{Hydrochar} + \text{Liquid} + \text{Gas} \quad (3)$$

The mass yield of the solid or hydrochar produced during HTC for time (dα/dt), depends on the rate of reaction constants, which are influenced by temperature [k(T)] and reaction model [f(α)], expressed as:

$$\frac{d\alpha}{dt} = k(T).f(\alpha) \quad (4)$$

where k(T) is the reaction rate constant depending on the temperature, f(α) is the function of α, and α is the conversion or weight loss rate that can be calculated with the following equation:

$$\alpha = \frac{m_{bio} - m_{HC_T}}{m_{bio} - m_{HC_\infty}} \quad (5)$$

where m_{bio} (g), is the initial weight of the sample, m_{HC_T} (g) is the weight of the sample at a given temperature and time, and m_{HC_∞} (g) is the final sample weight. The solid conversion rate (dα/dt) can be expressed as:

$$\frac{d\alpha}{dt} = \beta \frac{d\alpha}{dT} = k(T).f(\alpha) \quad (6)$$

where β is the heating rate or the rate of temperature change (dT/dt, K/min).

The kinetic parameters were determined using two HTC temperature zones (150-210 °C and 210-250 °C). For each temperature range, the biomass samples were subjected to three heating powers (160, 200 and 240 W). These powers correspond to different average value of β depending on the temperature zone. In the first zone, the β values corresponding to the powers were 1.8, 2.3 and 3 ºC/min, while in the second zone the β values were 0.7, 1.25 and 1.8 ºC/min. The continuous decrease of β value for the duration of the experiment at the same power is due to heat loss. However, for each power in the given temperature range, the value of β can be considered constant. As shown in **Fig. 1**, the temperature profile as a function of time at 150-210 ºC; and 210-250 ºC, can be considered as straight lines with $R^2 > 0.983$ for each.

The k(T) can be described according to the Arrhenius equation:

$$k(T) = A.e^{\frac{-E\alpha}{RT}} \quad (7)$$

where A (min^{-1}) refers to the pre-exponential factor, and Eα (J/mol) is the apparent activation energy, T (K) represent the absolute temperature, and R universal gas constant (8.314 J/ (mol·K)), respectively. Substituting Eq. (7) into (6) gives the following equation:

$$\frac{d\alpha}{dt} = \beta \frac{d\alpha}{dT} = A.e^{\frac{-E\alpha}{RT}}.f(\alpha) \quad (8)$$

The integral form of f (α) can be obtained after integrating Eq. (8) with respect to temperature.

$$g(\alpha) = \int_0^\alpha \frac{d\alpha}{f(\alpha)} = \frac{A}{\beta}\int_{T_0}^{T} e^{\frac{-E\alpha}{RT}} dT \quad (9)$$

where g(α) is the integrated reaction model, and some common forms of f (α) and g (α) for solid-state reactions are described in **Table 2**.

Table 2: Expressions for functions f(α) and g(α) of some reaction models to describe thermal decomposition solid state reactions [34]

Symbols	Reaction models	Differential form f(α)	Integral form g(α)
		Reaction order models	

R1	First order	$1-\alpha$	$-\ln(1-\alpha)$
R2	Second order	$(1-\alpha)^2$	$(1-\alpha)^{-1}-1$
R3	Third order	$(1-\alpha)^3$	$[(1-\alpha)^{-2}-1]/2$
R4	One and half order	$(1-\alpha)^{3/2}$	$\left[(1-\alpha)^{-1/2}-1\right]$
	Diffusion models		
D1	1D diffusion	$1/2\alpha$	α^2
D2	2D diffusion-Valensi	$[-\ln(1-\alpha)]^{-1}$	$(1-\alpha)\ln(1-\alpha)+\alpha$
D3	3D diffusion-Jander	$(1-\alpha)^{3/2}/\left[1-(1-\alpha)^{1/3}\right]$	$\left[1-(1-\alpha)^{1/3}\right]^2$
D4	3D diffusion-Ginstling	$(3/2)/\left[(1-\alpha)^{-1/3}-1\right]$	$1-2\alpha/3-(1-\alpha)^{2/3}$
	Power law nucleation Models		
P1	Power law (1)	$(2/3)\alpha^{-1/2}$	$\alpha^{3/2}$
P2	Power law (2)	$2\alpha^{1/2}$	$\alpha^{1/2}$
P3	Power law (3)	$3\alpha^{2/3}$	$\alpha^{1/3}$
P4	Power law (4)	$4\alpha^{3/4}$	$\alpha^{1/4}$
	Random nucleation and subsequent growth Models		
A1	Avrami-Erofeev (1)	$(3/2)(1-\alpha)[-\ln(1-\alpha)]^{1/3}$	$[-\ln(1-\alpha)]^{2/3}$
A2	Avrami-Erofeev (2)	$2(1-\alpha)[-\ln(1-\alpha)]^{1/2}$	$[-\ln(1-\alpha)]^{1/2}$
A3	Avrami-Erofeev (3)	$3(1-\alpha)[-\ln(1-\alpha)]^{2/3}$	$[-\ln(1-\alpha)]^{1/3}$
A4	Avrami-Erofeev (4)	$4(1-\alpha)[-\ln(1-\alpha)]^{3/4}$	$[-\ln(1-\alpha)]^{1/4}$
A5	Random nucleation (1)	$(1-\alpha)^2$	$1/(1-\alpha)$
A6	Random nucleation (2)	$(1-\alpha)^3/2$	$1/(1-\alpha)^2$
	Geometrical contraction models		
F1	Contracting area	$2(1-\alpha)^{1/3}$	$1-(1-\alpha)^{1/2}$
F2	Contracting volume	$3(1-\alpha)^{2/3}$	$1-(1-\alpha)^{1/3}$

The kinetics of thermal reactions in solids has been widely studied in the literature [34]. There are two main methods to determine the kinetic parameters, the model-free methods, and the model-fitting method.

2.5.1 Model-free method

The model-free method has been used in the pyrolysis, gasification, and combustion kinetic model and allows the kinetic parameters to be calculated as a function of the degree of conversion. Different methods have been used, such as the differential method proposed by Friedman and the integral methods, such as the FWO method and KAS method [46-48].

Friedman method: The Friedman method is the most common differential isoconversion method for determining activation energy as a function of conversion α, and it is given in the following equation:

$$\ln\left(\frac{d\alpha}{dt}\right) = \ln\left(\beta\frac{d\alpha}{dt}\right) = \ln[A_\alpha\, f(\alpha)] - \frac{E\alpha}{RT} \quad (10)$$

Ea can be obtained from the slope of the fit line drawn between $\ln\left(\beta\frac{d\alpha}{dt}\right)$ versus $\frac{1}{T}$.

FWO method: This method is derived from the integral isoconversional method. The method uses the linear Doyle's approximation for the estimation of temperature integral [35], and it is given in the following equation:

$$\ln\beta = \ln\frac{AE\alpha}{Rg(\alpha)} - 5.331 - 1.052\frac{E\alpha}{RT} \quad (11)$$

Plots of ln β vs. 1/T, at fixed value of conversion help in evaluating the activation energy from the slope of straight-line plot.

KAS method: The KAS method is based on the Coats–Redfern approximation and it is given in the following equation:

$$\ln\frac{\beta}{T^2} = \ln\frac{AR}{E\alpha\, g(\alpha)} - \frac{E\alpha}{RT} \quad (12)$$

For a constant value of α, the activation energy Eα can be obtained from the plot of $\ln\frac{\beta}{T^2}$ against $\frac{1}{T}$ with – Eα/R as the slope.

Several solid-state kinetic models have been discussed in the literature, and many different reaction mechanisms have been proposed to describe solid-state reactions, some of which are listed in **Table 2**. The models can be expressed in a differential form f(α) and an integral form g(α). The most used reaction mechanisms are described below.

2.5.2 Model-fitting methods

Model-fitting methods are commonly applied because the kinetic parameters can be determined and provide information about possible reaction mechanism models. The Coats-Redfern method, the most popular form of model-fitting, proposed in 1964 [36], uses Taylor's series approach by limiting the number of terms in the series. The Taylor series expansion form can be given as:

$$g(\alpha) = \int_0^{\alpha}\frac{d\alpha}{f(\alpha)} = \frac{A}{\beta}\int_{T_0}^{T} e^{\frac{-E\alpha}{RT}}dT = \frac{AE\alpha}{\beta R}\int_x^{\infty}\frac{e^{-x}}{x^2}dx \quad (13)$$

$$g(\alpha) = \frac{AE\alpha}{\beta R}\int_x^{\infty}\frac{e^{-x}}{x^2}dx \cong \frac{AE\alpha}{\beta R}\left[\frac{e^{-x}}{x^2}\left(1 - \frac{2!}{x} + \frac{3!}{x^2} - \frac{4!}{x^3} + \cdots\right)\right] \quad (14)$$

$$\frac{AE\alpha}{\beta R}\left[\frac{e^{-x}}{x^2}\left(1 - \frac{2!}{x} + \frac{3!}{x^2} - \frac{4!}{x^3} + \cdots\right)\right] = \frac{AE\alpha}{\beta R}p(x) \quad (15)$$

where x is equal to $\frac{E\alpha}{RT}$, the p(x) is the temperature integral and it has no analytical solution. Therefore, **Eq.(15)** can only be solved using either numerical integration or approximation to deal with the complex integral. By introducing an approximation $p(x)=x^{-2}e^{-x}$ ($20 \leqslant x \leqslant 50$) into **Eq. (14)**, the relationship between heating rate and inverse temperature becomes:

$$g(\alpha) = \frac{ART^2}{\beta E\alpha}\left(1 - \frac{2RT}{E\alpha}\right)e^{\frac{-E\alpha}{RT}} \quad (16)$$

Taking the natural logarithm of both sides of **Eq.(16)**.

$$\ln\frac{g(\alpha)}{T^2} = \ln\frac{AR}{\beta E\alpha}\left(1-\frac{2RT}{E\alpha}\right)-\frac{E\alpha}{RT} \quad (17)$$

Since 2RT/Ea << 1, the equation can be converted into

$$\ln\frac{g(\alpha)}{T^2} = \ln\frac{AR}{\beta E\alpha}-\frac{E\alpha}{RT} \quad (18)$$

For a fixed β and proposed reaction mechanism g(α), plotting $\ln\frac{g(\alpha)}{T^2}$ versus $\frac{1}{T}$ gives a straight line. The equations corresponding to g(α) are presented in **Table 2**. The slope −Eα/R and intercept $\ln\frac{AR}{\beta E\alpha}$ can be used to determine Eα and A, respectively [37].

2.5.3 Kinetic reaction mechanism models

All kinetic reaction mechanism models used in this study are presented in **Table 2**. Most solids contain different defects, weak points that can initiate physical and chemical changes during their reaction. These defects play an essential role when nucleation is the limiting step in a reaction [38]. If the reaction involves random nucleation followed by the growth of nuclei of a defined dimensionality, the Avrami-Erofeev equation can be derived and applied; in some cases, the nucleation rate follows the power law [37, 39]. In other cases, the solid-state reactions, are controlled by diffusion of the reagents or products. This situation is not common because the mass transfer in the solid-state is slower [39, 40]; however, in HTC processes, where one of the most important reactions is hydrolysis [23, 41], which modifies the biomass structure, the diffusion of water into the pores of the biomass particles can control the reaction mechanisms. This phenomenon was explained by Reza et al. [42]. Some solid-state reactions involve two or more substances, where phase boundaries are formed between the reagents and the products. In this case, the advance in the phase boundary thus formed determines that reaction rate [38]. When the advancement of the phase boundary is one-dimensional, a reaction of zero-order is obtained; if the phase boundary is two-dimensional the contracting area models is generated and if the phase boundary is three-dimensional, the contracting volume is obtained [43]; these models are based on the assumption of spherical solid particles. Finally, the kinetics of the solid-state reaction can be controlled by the order of the reaction. These models are the simplest as they are similar to those used in homogenous kinetics [24, 44]. Often, first and second-order reactions are used. Higher-order reactions are rarely used and difficult to interpret in solid-state reactions [38].

3 RESULTS AND DISCUSSION

3.1 Mass yield and derivative mass yield analysis

The Y_{HC} and DY_{HC} curves of the AS at different powers applied in the reactor corresponding to different heating rates are shown in **Fig. 2a.** The evolution with the temperature at different heating rates of Y_{HC} is calculated based on the **Eq.(1)** at different temperatures. Four distinct zones can be identified in the **Fig. 2a**. Up to 160 °C, initial induction period is observed in which the reaction rate is quite slow (first zone). In this period, the energy in the reaction medium is not high enough to reach activation energy. The reaction starts in the second zone, at a temperature of ~160 °C; in this zone, the maximum rate of biomass decomposition is observed, and it is finished at approximately 200 °C.

This decrease in mass yield is due to decomposition reactions of biomasses, such as hydrolysis, dehydration, decarboxylation, and so forth [41]. The hydrolysis breaks down the biomass chemical structure through cleavage of ester and ether bonds of bio-macromolecules with water molecules. This process creates (oligo-) saccharides and fragments of lignin that enter the liquid phase [45, 46] thus reducing the total solid yield, as shown in **Fig. 2a**. The hydrolyzed products can degrade into furfurals, particularly 5-hydroxymethylfurfural, aldehyde, erythrose, and with undergo dehydration and decarboxylation [47]. Dehydration removes water from the biomass matrix without changing its chemical constitution, evidenced by the increased carbon contents and decreased oxygen contents. Decarboxylation involves the degradation of hemicellulose and cellulose; these materials can degrade into monomers, such as acetic acid, formic acid, lactic acid, and furfurals further degrade into CO_2 and H_2O [42]. The decarboxylation reaction removes carboxyl and carbonyl groups. Carboxyl and carbonyl groups rapidly degrade above 150-180 °C, yielding CO_2, and CO, respectively [48]. All these reactions mentioned above are decomposition reactions, causing a decrease in the total solid yield and increasing the liquid and gas production. The low decomposition temperature of this biomass can be related to its high content of hemicellulose (76.4%) or biomolecules with solubilities similar to that of hemicellulose. Other reaction mechanisms of HTC are aromatization and polymerization. HTC increases the production of aromatics from intermediates products formed during hydrolysis [42]. Moreover, lignin is composed of many aromatic compounds polymerized by various linkages. Hydrochar produced during HTC is a cross-linked polymer and has similar properties to lignin, so

hydrochar is almost impossible to distinguish from the unreacted lignin fraction. Also, a polymer, such as cellulose and hemicellulose can be converted into a cross-linked polymer similar to lignin [49, 50].

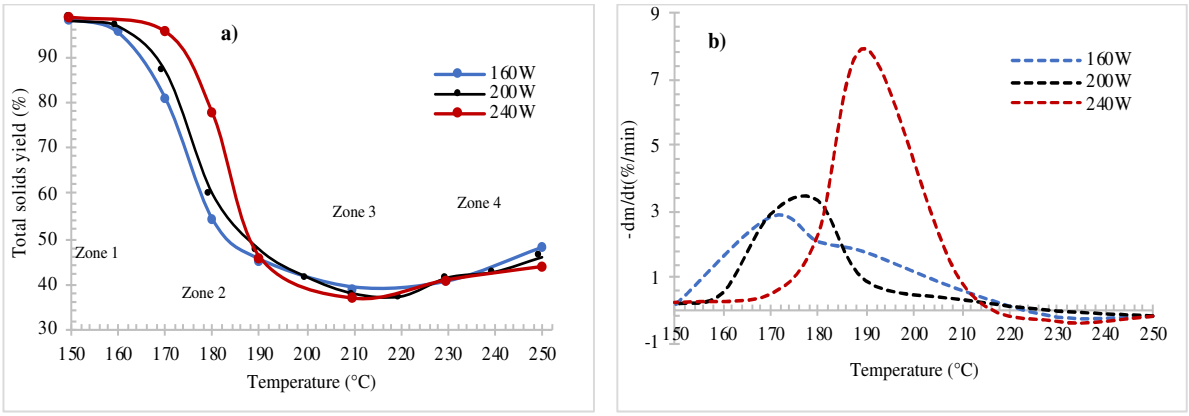

Fig. 2: Evolution with temperature, **a)** the total solids yield (Y_{HC}), b) and derivative of total solids yield (DY_{HC}) at different power (160, 200 and 240W).

The stability of the aromatic structures is a basic element in the hydrochar formation. This stability is observed in zone 3, between 200 and 220 °C, as shown in **Fig. 2a**. The intermediates of unsaturated compounds such as aldehydes, furfural, and 5-HMF produced from dehydration and decarboxylation reactions are highly reactive. These monomers are followed by condensation, polymerization, and aromatization to form S-HC [5, 42]. The S-HC formation increases the total solid yield, as shown in zone 4 in **Fig. 2a,** between 220 and 250 ºC. Similar increases of the total solid yield were observed by Yang et al. [51] during the cellulose carbonization at a temperature above 275 °C. The inclusion of a stirrer in the reactor helps obtain a uniform biomass/water mixture inside the reactor, avoiding concentration or temperature gradients inside the reactor; this may increase the reaction mechanisms in the HTC process. The increased reaction mechanism can lead to rapid polymerization of the intermediates of unsaturated compounds produced from dehydration and decarboxylation.

The heating rate is an essential factor during the thermochemical conversion process of biomass since it affects the process through a heat transfer and mass transfer through the biomass particles. In the **Fig. 2**, the Y_{HC} and DY_{HC} are represented at various heating rates. However,

354 DY_{HC} curve (**Fig. 2b)** became sharper as the heating rate increased. Higher heating rates
355 significantly enhanced total solid yield loss rates than those by the lower heating rates.
356 **Fig. 2b** shows that the peaks of DY_{HC} curves slightly shifted to the right as the heating rate
357 increased this can be explained by the fact that the gradient temperature of a particle and
358 distribution of temperature was smaller at low heating rates. The maximum decomposition peaks
359 were observed of 174, 182, and 189 ºC for a power of 160, 200, and 240 W, respectively.

360 **3.2 Secondary hydrochar analysis.**

361 The condensation, polymerization, and aromatization reactions form secondary hydrochar on the
362 surface of the primary hydrochar. This secondary hydrochar is derived from the decomposition
363 of hemicellulose, and cellulose, followed by polymerization of intermediates product into
364 amorphous carbonaceous compounds during HTC. The increase in temperature and time of HTC
365 gradually increases the amorphous carbon, such as aliphatic and aromatic groups on the surface
366 of the primary hydrochar [52]. The condensation of amorphous carbon on the primary hydrochar
367 surface during HTC results in the retention of PAHs [20]. This secondary hydrochar was
368 extracted from the total solids produced at 190, 210, 230, and 250 °C at a heating power of 1.5
369 ºC/min by extracting Soxhlet with toluene (100%). Extraction was also done with raw biomass.
370 The amount extracted in the hydrochar structures and the raw biomass is presented in **Table 3**. It
371 was noteworthy to note that a significant increase in secondary hydrochar removed in total
372 solids produced was observed when the temperature was above 190 ºC; this explains the increase
373 in total solid yield or total hydrochar as explained in **section 3.1**, **Fig. 2**. The analyses of liquid
374 solutions of secondary hydrochar and biomass extractive compounds show different aliphatic
375 and PAHs compounds.

376 **Table 3:** The secondary hydrochar removed in total solids yield at different HTC temperatures.

HTC-Temperature	Extracted secondary hydrochar. (wt.%)
AS_250ºC	19.01
AS_230ºC	13.86
AS_210ºC	10.05
AS_190ºC	5.48
Raw_AS	3.80

3.2.1 Aliphatic content analysis

The long-chain aliphatic hydrocarbons that were found are shown in **Fig. 3**. During HTC, a series of reactions of the coalification occurred. The oxygenated hydrocarbons are initially converted to aliphatic (alkanes, olefins) and aromatics compounds and then transformed to higher hydrocarbons and larger PAHs with a further increase in temperature [17]. The high molecular weight hydrocarbons, which were found in the S-HC solution, include long chain alkanes, such as tetradecane (RT ≈8.9min), pentadecane (RT ≈10.1min), hexadecane (RT ≈ 11.3min), heptadecane (RT ≈ 12.4min), octadecane (RT ≈ 13.5min), and eicosane (RT ≈ 14.6min). The signal of these aliphatic compounds increases with increasing temperature, and it was not detected in the S-HC solution removed from the raw biomass.

The main olefin of high molecular weight detected was 9-octadecenoic acid (oleic acid), an 18-carbon monounsaturated fatty acid (RT ≈ 34.3min). Also, it was detected 9-octadecenamide (RT≈ 29.7min), an amide derived from oleic fatty acid. All these compounds were detected in all the hydrochars produced. The intensity of the peaks increases, with the increase of the temperature, they confirm the formation of tars on the hydrochar structure. The condensation of these aliphatic compounds on hydrochar surface results in retention of PAHs [20]. Unlike the hydrochar produced, the components that were detected in the raw biomass extractable were mainly fatty acids, such as stearic acid (RT ≈ 19.20min) and (11E)-11-octadecenoic acid (RT≈ 19.83min).

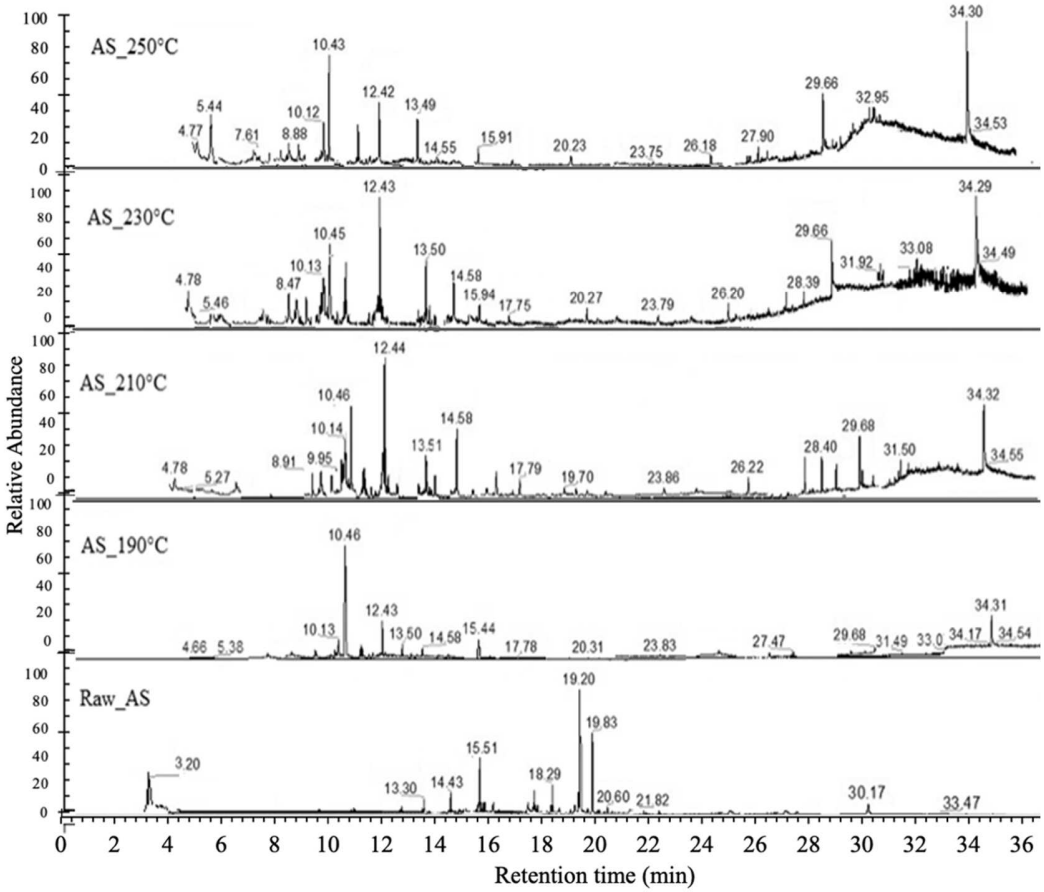

Fig. 3: The main aliphatic compounds detected in secondary hydrochar solution removed in the hydrochar structure and raw AS.

3.2.2 PAHs content analysis.

The chromatogram of total PAHs in hydrochar and raw AS are presented in **Fig. 4**. The results showed that total PAHs in the hydrochars were higher than those in raw AS. The PAHs detected in the raw biomass was bibenzyl (RT≈ 30.98min), the simplest PAHs (2 rings). The peak with a retention time of 17 and 23min are benzaldehyde and Benzyl alcohol, respectively. The number of PAHs detected in the hydrochars increases with increasing temperature; this may be explained by polymerization and aromatization reactions during the HTC process. At the lower temperature of HTC (190ºC and 210ºC), the PAHs detected were mainly 2-3 rings.

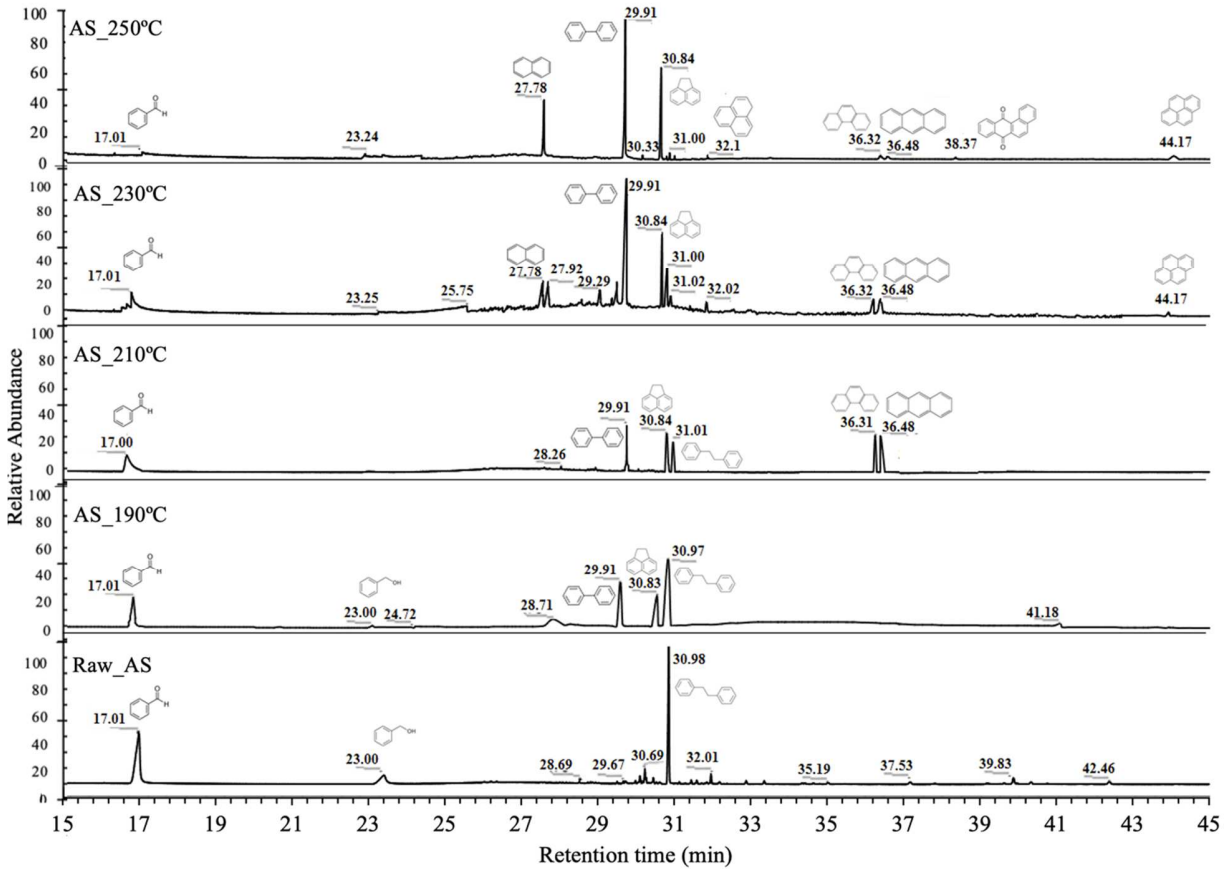

Fig. 4: The main PAHs compounds detected in secondary hydrochar solution removed in the hydrochar structure and raw AS.

The 2-ring were biphenyl, bibenzyl, and naphthalene with the retention time of 29.91, 31 and 27.78min respectively. The PAHs with 3 rings detected were acenaphthene, phenanthrene, and anthracene with retention times 30.84, 36.32, and 36.48min, respectively. In addition to the fact that all these mentioned PAHs were detected at a high temperature of HTC (230 and 250 °C), other PAHs were detected, such as 4-methyl biphenyl, acenaphthene, cis-stilbene, 1H-phenalene, and pyrene, with the retention time of 30.33, 31.07, 31.22 32.1, and 44.17 min respectively. At a temperature of 250ºC, another 4-ring oxygenated PAHs was detected, such as 7,12-dihydrobenzo[a]antracene, with the retention time of 38.37min. At low temperatures, the biomass was subjected to initial hydrolysis, dehydration, and depolymerization reaction [47], which led to a decrease in total PAHs because the polymerization and aromatization reaction have not started.. The intermediates unsaturated compounds produced from dehydration and decarboxylation promoted PAHs formation with increasing temperature by aromatization and

polymerization reactions, so increasing the PAHs rings formed. The hydrochars obtained at temperatures from 190 to 210 °C, biphenyl and bibenzyl (2 rings) were dominant while phenanthrene, Anthracene, and Pyrene were most prevalent at high HTC temperature (230 - 250 °C).

3.3 Kinetic analysis results

Thermal analysis methods are currently used to determine the reactivities and mechanisms of thermal reactions of solids. Estimation of kinetic parameters involves activation energy and pre-exponential factor. This study proposes different model-free methods, such as FWO, KAS, and Friedman to determine AS kinetic parameters during HTC. Although model-free methods can reliably estimate the kinetic parameters, the information obtained is limited, It do not allow to define the reaction mechanism unlike model-fitting methods [53].

3.3.1 Model-free method

In this study, model-free methods first analyzed the kinetics of the HTC of AS. Starting from **Eq. (** 5) and applying above mentioned isoconversional methods. The activation energy (Eα), pre-exponential factor (A), and linear correlation coefficient (R^2) at various conversion rates of 0.1–0.9 were calculated using the FWO, KAS, and Friedman methods. The calculated average values of Eα, A, and R^2 are shown in **Table 4**. These parameters were calculated in two zones of HTC temperature. The first zone corresponds to the decrease in the Y_{HC} between 150 and 210 °C, and the second zone corresponds to the increase of the Y_{HC} from 210 to 250 °C where appears formation of heavy PAHs

Table 4: Kinetic parameters of AS determined by the model-free kinetics methods.

Temperature (°C)	FWO			KAS			Friedman		
	Eα (kJ/mol)	A (min^{-1})	R^2	Eα (kJ/mol)	A (min^{-1})	R^2	Eα (kJ/mol)	A (min^{-1})	R^2
150-210	89.61±12.19	$7.55x10^{9}$	0.982	86.79±12.82	$3.39x10^{9}$	0.979	73.81±35.47	$2.24x10^{12}$	0.630
210-250	181.28±20.13	$78x10^{-19}$	0.909	199.12±21.16	$1.38x10^{-19}$	0.916	223.27±31.56	$2.49x10^{-6}$	0.801

As shown in **Table 4**, the Eα values obtained for the integral methods (FWO and KAS) are similar and show the best fit correlation coefficient (R^2) compared to the differential method (Friedman). The Friedman method requires derivative conversion data, which would lead to being numerically unstable and noise-sensitive [54]. For this reason, in general, the integral methods show the best-fit correlation coefficient values than the differential method.

In the first zone, the HTC temperatures were between 150 and 210 °C. The average Eα values were 89.61±12.19 kJ/mol, 86.79±12.82 kJ/mol. The small differences observed in Eα values obtained using KAS and FWO can be assigned to the different approximations of the temperature integral. In **Fig. 5a**, it can be observed that the values of Eα are not similar for all conversion values, indicating the existence of a complex multi-step mechanism reaction that occurs in the biomass HTC process. The progressive variation of Eα values could correspond to competitive or consecutive reactions and the multiphasic biomass conversion. For α values from 0.1 to 0.6, a decrease of Eα from 99 to 68 kJ/mol. However, from 0.6, an increase of Eα is observed; this may be due to the change of the mechanism of chemical reactions. In this range of HTC temperature, similar values of Eα were reported by Killer et al. [26] for cellulose and hemicellulose using the nonlinear least-square minimization method. The values obtained were 61 kJ/mol and 127 kJ/mol for hemicellulose and cellulose. Also, Danso-Boateng et al. [55] reported the value of activation energy (77.8 kJ/mol, with pre-exponential factor $1.5x10^7$ min^{-1}) for synthetic feces and 70.4 kJ/mol, with a pre-exponential factor of $4.0x10^6$ min^{-1} for primary sewage sludge.

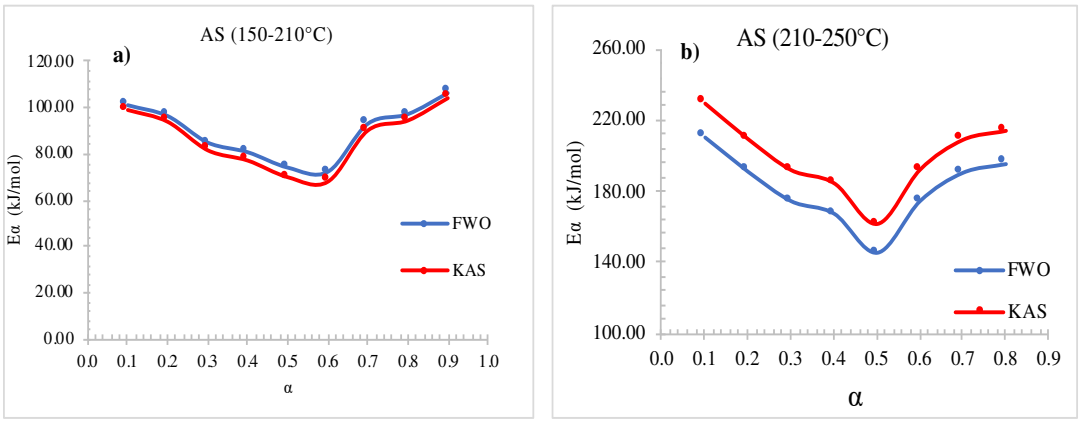

Fig. 5: Eα values according to the degree of conversion (α) for HTC process of (a) 150 to 210 °C and (b) 150 to 210 °C of HTC temperature according to the FWO and KAS.

In the second zone (210 to 250 °C), they corresponded to an increase in Y_{HC} for AS. The Eα values are displayed in **Table 4** and **Fig. 5b**. The values obtained are a similar trend for integral methods.

As in the previous one, there is also a change in the trend of Eα showing a complex multi-step mechanism reaction. The values of Eα vary from 145.28 to 210.74 kJ/mol and 245.28 to 229.95

kJ/mol for FWO and KAS respectively. As a comparison, the FWO and KAS method was more reliably attributed to its higher R^2 values. The high Eα values obtained in this temperature zone are due to the condensation, polymerization, and aromatization reactions. This reaction occurs at higher temperatures and reaction times [5]. In this temperature range (205-245 °C), Yang et al. [51] reported values of 226.5 kJ/mol of HTC for cellulose.

As shown in **Fig. 5**, the different Eα express different reaction mechanisms. The model-fitting methods can explain the different models for each stage of conversion.

3.3.2 Model-fitting method

The model-fitting method applied in this study was the Coats-Redfern method; this method enabled the determination of the kinetic parameters, i.e., activation energy and kinetic model (g(α)). In **Table 5**, the average activation energy of different heating rates is displayed to identify the kinetic reaction model of the HTC process for AS. As shown in **Table 5**, the Eα values determined are somewhat mildly variable when changing the reaction model and can be really different to the value obtained with model-free method.

Table 5: Kinetic parameters of AS determined by model-fitting method in HTC process for AS

	150-210°C		210-250°C	
Model-Symbols	$E\alpha_{mean}$ (kJ/mol)	R^2_{mean}	$E\alpha_{mean}$ (kJ/mol)	R^2_{mean}
R1	148.84±4.93	0.968	**230.96±28.84**	**0.916**
R2	212.95±5.53	0.988	330.30±37.72	0.937
R3	292.87±6.57	0.977	453.89±48.76	0.928
R4	178.58±5.19	0.983	277.12±32.98	0.933
D1	214.92±8.94	0.909	329.16±44.61	0.853
D2	239.39±9.26	0.931	367.69±48.32	0.877
D3	270.92±9.55	0.953	417.00±52.85	0.902
D4	249.74±9.35	0.939	383.89±49.81	0.887
P1	159.32±6.70	0.907	244.76±33.45	0.85
P2	48.12±2.22	0.888	75.96±11.14	0.831
P3	29.59±1.48	0.87	47.83±7.42	0.813
P4	20.32±1.10	0.847	33.76±5.56	0.794
A1	**96.73±3.28**	**0.966**	151.16±19.22	0.913
A2	70.68±2.46	0.964	111.26±14.41	0.91
A3	44.63±1.64	0.96	71.36±9.60	0.903
A4	31.60±1.23	0.955	51.41±7.20	0.896
A5	101.75±2.32	0.903	161.50±16.08	0.87

A6	210.98±4.59	0.869	331.44±32.16	0.906
F1	48.12±2.22	0.888	75.96±11.14	0.831
F2	29.59±1.48	0.87	47.83±7.42	0.813

The main hypotheses that can explain the inconsistency Eα values between the model-free and model-fitting methods are the model-free model assumes that the reaction mechanism is first-order. However, there may be different mechanisms during the conversion process. These mechanisms can be explained for the model-fitting. Also, to determine the kinetic parameter for model-free method, at least three heating rates are required. On the other hand, only one heating rate value is necessary for the model-fitting to estimate the kinetic parameters. In most biomass thermal degradation works in literature, the chosen kinetic model is the reaction first order ($f(\alpha)=1-\alpha$), even if each phase could be described as a different model. In this case, if the mean value of Eα for different heating rates at a specified conversion range based upon one particular model is closest to the value by the model-free methods, in addition to the high correlation coefficients (R^2), then this model may dominate the reactions in this range [56, 57].

The calculated Eα at different heating rates is shown in **Fig. 6** and **Fig. 7**. It can be seen in **Fig. 6** that for the reaction order model series, the estimated average value of Eα for the cases of the three heating rates varies from 148.8 kJ/mol to 292.87kJ/mol. But none of the estimated average Eα based upon this series reaction model is close to 89.61 kJ/mol. Although higher correlation values are obtained for this model series ($R^2 > 0.968$), the Eα values obtained are much greater than those of the free models values.

In fact, the reaction model corresponding to Avrami-Erofeev (1) gives a similarity Eα values with model-free methods in the temperature between 150 and 210ºC indicate that the HTC kinetics of AS follows a random nucleation model ($g(\alpha) = [-\ln (1-\alpha)]^{2/3}$). The kinetic transformations of Avarami-Erofeev models usually follow a characteristic sigmoidal profile (S-shape) where the transformation rates are low at the beginning and the end of the transformation but rapid in between; this explains the shape of the curve in **Fig. 2a**. A similar observation was reported by Álvarez-Murillo et al. [58] in the HTC process for the cellulose decomposition curve.

However, in the second zone (210 to 250°C) corresponding to an increase in Y_{HC}, the best model giving the value close to $E\alpha_{FWO}$ (181.28 kJ/mol) is the first order model (R1) as shown in **Fig. 7**. The estimated average value of Eα varies from 199.26 kJ/mol to 255.65 kJ/mol. The first-order

reaction model may be the most appropriate model to express the HTC process of AS in this temperature range.

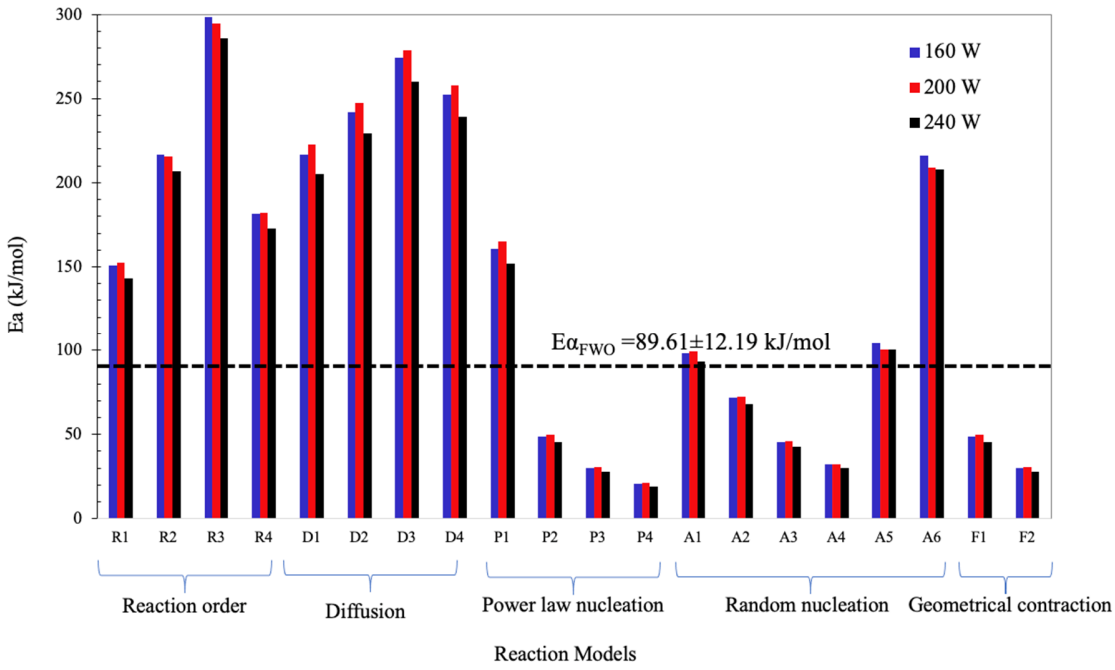

Fig. 6: Comparison of kinetic parameters from model-fitting methods of temperature between 150 and 210ºC

Although model-free methods were generally regarded as reliable ones, they can calculate both Eα and A values. However, this method is based on supposed first-order reaction models, and the thermal decomposition can follow different reaction models, which are not necessarily first-order model reactions, as demonstrated for AS HTC temperature between 150 and 210 ºC. On the other hand, model-fitting methods have enabled the determination of the kinetic model (g(α)), also activation energy (Eα), but any list of the model-fitting method is certainly incomplete, and it is entirely possible that the studied process is not described by any of them [54].

Moreover, this method depends on the heating rate and range of conversion. As shown in **Fig. 7**, Ea values increased with increasing heating rate. This phenomenon is because as the heating rate increased, it led to a sharp increase in intermediates reaction rates and lower activation energies. Similar results were observed by Mui et al. [59] in the pyrolysis of cellulose, hemicellulose, and lignin.

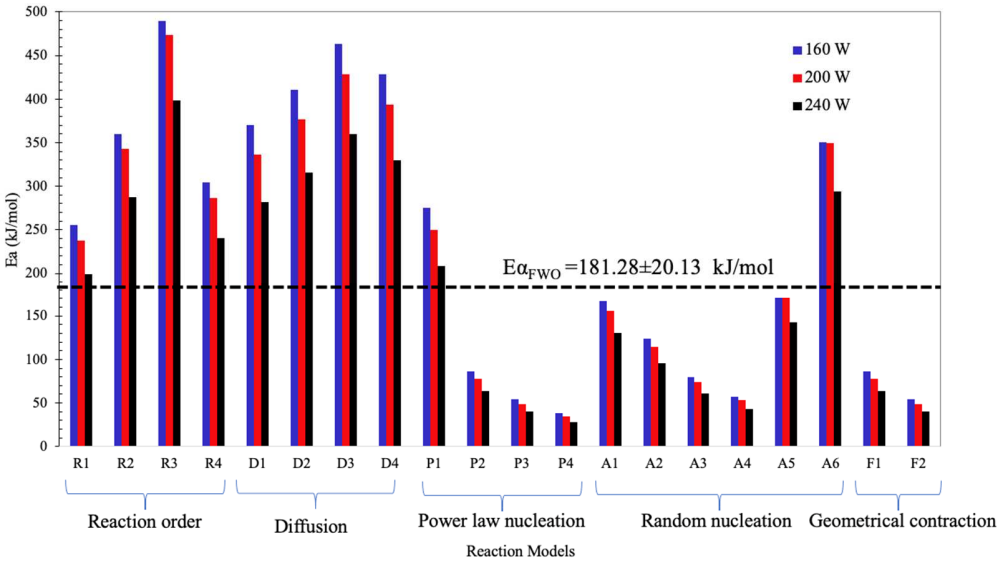

Fig. 7: Comparison of kinetic parameters from model-fitting methods of temperature between 210 and 250ºC

Consequently, it was recommended that model-fitting methods and model-free methods support each other to investigate the HTC mechanism. Therefore, according to comparing the model-free and model-fitting methods' activation energy, the random nucleation (Avrami-Erofeev-1) model may be considered the most suitable model to characterize the HTC of AS in the range of 150ºC to 210°C. Simultaneously, a temperature between 210 and 250ºC follows a first-order reaction model.

Conclusions:

This study is focused on kinetic studies of hydrothermal carbonization of avocado stone, using different temperature and time conditions. The kinetics of the process was studied using different models and methods (model-free and model-fitting methods). The following conclusions can be drawn from the results of the study:

According to the analysis of total solids yield, the HTC of the AS can be divided into four main zones. Initial induction period in the first zone in which the reaction rate is relatively slow (up to 160°C), followed by a maximum loss of total solid yield up to 200ºC. The third zone corresponds to the stabilization zone, dominated by condensation reactions; this stability is observed between 200 and 220°C. The last zone is the increase in the total solid mass yield. The increase of the

552 total solid mass yield between 220 and 250ºC is related to the aromatization and polymerization
553 reactions. This increase was confirmed with the Soxhlet extraction and analysis of the secondary
554 hydrochars (tars) formed. The increase in temperature of HTC gradually increases the tars
555 compounds, such as aliphatic and PAHs on the hydrochar.
556 The results of GC–MS analysis of the secondary hydrochar solution indicate that it contains
557 aliphatic and PAHs components. The aliphatic compounds detected were mainly characterized
558 by long-chain alkanes and some unsaturated fatty acids. The number and weight of PAHs
559 increase with the increasing temperature of HTC. The most abundant PAHs were two and three-
560 ring. However, 4-ring PAHs were detected in low numbers in hydrochars produced at 230 and
561 250ºC.
562 The decomposition of avocado stone during the HTC in temperatures range between 150 and
563 210°C follows a random nucleation reaction mechanism (Avrami-Erofeev-1) whereas in the
564 temperature between 210 and 250 follows a first-order reaction model. The average activation
565 energy estimated for Avrami-Erofeev-1 was 96.73±3.28 kJ/mol. The values obtained from FWO
566 and KAS are consistent with Avrami-Erofeev-1, where the activation energies are 89.61±12.19
567 kJ/mol and 86.79±12.82 kJ/mol, respectively. The average activation energy estimated for the
568 first-order reaction model is 230.96±28.84 kJ/mol. The best values obtained for the model-free
569 method were between 145-210 kJ/mol and 161-229 kJ/mol for the FWO and KAS methods.
570 Moreover, the values of activation energies at different conversions have indicated the multi-
571 reaction scheme's existence during the HTC of avocado stone.

572 **Acknowledgments**

573 The authors are grateful to CONACYT (Consejo Nacional de Ciencia y Tecnología de México)
574 for granting the scholarship No. 659624 for this research. Also, we are grateful to ICARE -
575 CNRS- France and the Région Centre-Val de Loire for financial support within the INFLUX
576 project.
577

578 **References**

579 1. Czernik S, Bridgwater A. Overview of applications of biomass fast pyrolysis oil. Energy & fuels
580 2004; **18**(2): 590-598
581 2. Funke A, Ziegler F. Hydrothermal carbonization of biomass: a summary and discussion of
582 chemical mechanisms for process engineering. Biofuels, Bioproducts and Biorefining 2010; **4**(2):
583 160-177

3. Kim D, Lee K, Park K Y. Hydrothermal carbonization of anaerobically digested sludge for solid fuel production and energy recovery. Fuel 2014; **130**: 120-125

4. Missaoui A, Bostyn S, Belandria V, Cagnon B, Sarh B, et al. Hydrothermal carbonization of dried olive pomace: Energy potential and process performances. Journal of Analytical and Applied Pyrolysis 2017

5. Sevilla M, Fuertes A B. The production of carbon materials by hydrothermal carbonization of cellulose. Carbon 2009; **47**(9): 2281-2289

6. Sabio E, Álvarez-Murillo A, Román S, Ledesma B. Conversion of tomato-peel waste into solid fuel by hydrothermal carbonization: Influence of the processing variables. Waste management 2016; **47**: 122-132

7. Chen W-H, Ye S-C, Sheen H-K. Hydrothermal carbonization of sugarcane bagasse via wet torrefaction in association with microwave heating. Bioresource technology 2012; **118**: 195-203

8. Zhang L, Liu S, Wang B, Wang Q, Yang G, et al. Effect of residence time on hydrothermal carbonization of corn cob residual. BioResources 2015; **10**(3): 3979-3986

9. Álvarez-Murillo A, Román S, Ledesma B, Sabio E. Study of variables in energy densification of olive stone by hydrothermal carbonization. Journal of Analytical and Applied Pyrolysis 2015; **113**: 307-314

10. Alves B. Fresh avocado production in Mexico from 2013/14 to 2019/20. 2020; Available from: https://www.statista.com/statistics/591329/mexico-fresh-avocado-production/

11. Perea-Moreno A-J, Aguilera-Ureña M-J, Manzano-Agugliaro F. Fuel properties of avocado stone. Fuel 2016; **186**: 358-364

12. Salgado J M, Danieli F, Regitano-D'Arce M A B, Frias A, Mansi D N. The Avocado Oil (persea Americana Mill) As A Raw Material For The Food Industry [o óleo De Abacate (persea Americana Mill) Como Matéria-prima Para A Indústria Alimentícia]. Ciencia e Tecnologia de Alimentos 2008

13. Rodríguez-Sánchez D G, Pacheco A, García-Cruz M I, Gutiérrez-Uribe J A, Benavides-Lozano J A, et al. Isolation and structure elucidation of avocado seed (Persea americana) lipid derivatives that inhibit Clostridium sporogenes endospore germination. Journal of agricultural and food chemistry 2013; **61**(30): 7403-7411

14. McLeod L, Flores D. USDA-Foreing-Agricultural-Service (2017) Mexico Avocado Annual. 2017 [cited 2020 25/10]; Available from: https://www.fas.usda.gov/data/mexico-avocado-annual-2

15. Lucian M, Volpe M, Gao L, Piro G, Goldfarb J L, et al. Impact of hydrothermal carbonization conditions on the formation of hydrochars and secondary chars from the organic fraction of municipal solid waste. Fuel 2018; **233**: 257-268

16. Paksung N, Pfersich J, Arauzo P J, Jung D, Kruse A. Structural effects of cellulose on hydrolysis and carbonization behavior during hydrothermal treatment. ACS omega 2020; **5**(21): 12210-12223

17. Peng N, Li Y, Liu T, Lang Q, Gai C, et al. Polycyclic aromatic hydrocarbons and toxic heavy metals in municipal solid waste and corresponding hydrochars. Energy & Fuels 2017; **31**(2): 1665-1671

18. Wang L, Li A, Chang Y. Hydrothermal treatment coupled with mechanical expression at increased temperature for excess sludge dewatering: Heavy metals, volatile organic compounds and combustion characteristics of hydrochar. Chemical Engineering Journal 2016; **297**: 1-10

19. Malghani S, Gleixner G, Trumbore S E. Chars produced by slow pyrolysis and hydrothermal carbonization vary in carbon sequestration potential and greenhouse gases emissions. Soil Biology and Biochemistry 2013; **62**: 137-146

20. Al-Wabel M I, Rafique M I, Ahmad M, Ahmad M, Hussain A, et al. Pyrolytic and hydrothermal carbonization of date palm leaflets: Characteristics and ecotoxicological effects on seed germination of lettuce. Saudi journal of biological sciences 2019; **26**(4): 665-672

21. Wang T, Zhai Y, Zhu Y, Li C, Zeng G. A review of the hydrothermal carbonization of biomass waste for hydrochar formation: Process conditions, fundamentals, and physicochemical properties. Renewable and Sustainable Energy Reviews 2018; **90**: 223-247

22. Zeng X, Ueki Y, Yoshiie R, Naruse I, Wang F, et al. Recent progress in tar removal by char and the applications: A comprehensive analysis. Carbon Resources Conversion 2020; **3**: 1-18.

23. Kambo H S, Dutta A. A comparative review of biochar and hydrochar in terms of production, physico-chemical properties and applications. Renewable and Sustainable Energy Reviews 2015; **45**: 359-378

24. Ischia G, Fiori L. Hydrothermal Carbonization of Organic Waste and Biomass: A Review on Process, Reactor, and Plant Modeling. Waste and Biomass Valorization 2021; **12**(6): 2797-2824

25. Reza M T, Yan W, Uddin M H, Lynam J G, Hoekman S K, et al. Reaction kinetics of hydrothermal carbonization of loblolly pine. Bioresource technology 2013; **139**: 161-169

26. Keiller B G, Muhlack R, Burton R A, van Eyk P J. Biochemical Compositional Analysis and Kinetic Modeling of Hydrothermal Carbonization of Australian Saltbush. Energy & Fuels 2019; **33**(12): 12469-12479

27. Liu Z, Balasubramanian R. Hydrothermal carbonization of waste biomass for energy generation. Procedia Environmental Sciences 2012; **16**: 159-166

28. Pecchi M, Patuzzi F, Benedetti V, Di Maggio R, Baratieri M. Kinetic analysis of hydrothermal carbonization using high-pressure differential scanning calorimetry applied to biomass. Applied Energy 2020; **265**: 114810

29. Ceballos A M, Montoya S. Evaluación química de la fibra en semilla, pulpa y cáscara de tres variedades de aguacate. Biotecnología en el sector agropecuario y agroindustrial 2013; **11**(1): 103-112

30. Sangare D, Missaoui A, Bostyn S, Belandria V, Moscosa-Santillan M, et al. Modeling of Agave Salmiana bagasse conversion by hydrothermal carbonization (HTC) for solid fuel combustion using surface response methodology. aimspress energy 2020; **8**(4): 538-562

31. Sangare D, Bostyn S, Moscosa-Santillan M, Gökalp I. Hydrodynamics, heat transfer and kinetics reaction of CFD modeling of a batch stirred reactor under hydrothermal carbonization conditions. Energy 2020: 119635

32. Román S, Libra J, Berge N, Sabio E, Ro K, et al. Hydrothermal carbonization: modeling, final properties design and applications: a review. Energies 2018; **11**(1): 216

33. Hilber I, Blum F, Leifeld J, Schmidt H-P, Bucheli T D. Quantitative determination of PAHs in biochar: a prerequisite to ensure its quality and safe application. Journal of agricultural and food chemistry 2012; **60**(12): 3042-3050

34. Mumbach G D, Alves J L F, da Silva J C G, Di Domenico M, de Sena R F, et al. Pyrolysis of cocoa shell and its bioenergy potential: evaluating the kinetic triplet, thermodynamic parameters, and evolved gas analysis using TGA-FTIR. Biomass Conversion and Biorefinery 2020: 1-17

35. Doyle C D. Kinetic analysis of thermogravimetric data. Journal of applied polymer science 1961; **5**(15): 285-292

36. Coats A, Redfern J. Kinetic parameters from thermogravimetric data. Nature 1964; **201**(4914): 68-69

37. Yao Z, Yu S, Su W, Wu W, Tang J, et al. Kinetic studies on the pyrolysis of plastic waste using a combination of model-fitting and model-free methods. Waste Management & Research 2020; **38**(1_suppl): 77-85

38. Qiu Y, Chen Y, Zhang G G, Yu L, Mantri R V, Developing solid oral dosage forms: pharmaceutical theory and practice, in Book Developing solid oral dosage forms: pharmaceutical theory and practice. 2016, Academic press

39. Khawam A, Flanagan D R. Solid-state kinetic models: basics and mathematical fundamentals. The journal of physical chemistry B 2006; **110**(35): 17315-17328

40. Brown M E, Dollimore D, Galwey A K, Reactions in the solid state, in Book Reactions in the solid state. 1980, Elsevier

41. Volpe M, Goldfarb J L, Fiori L. Hydrothermal carbonization of Opuntia ficus-indica cladodes: Role of process parameters on hydrochar properties. Bioresource technology 2018; **247**: 310-318

42. Reza M T, Uddin M H, Lynam J G, Hoekman S K, Coronella C J. Hydrothermal carbonization of loblolly pine: reaction chemistry and water balance. Biomass Conversion and Biorefinery 2014; **4**(4): 311-321

43. Galwey A K, Brown M E, Thermal decomposition of ionic solids: chemical properties and reactivities of ionic crystalline phases, in Book Thermal decomposition of ionic solids: chemical properties and reactivities of ionic crystalline phases. 1999, Elsevier

44. Khawam A. Application of solid-state kinetics to desolvation reactions. The journal of physical chemistry B 2007; **210**(37): 1520-1545

45. Fang J, Zhan L, Ok Y S, Gao B. Minireview of potential applications of hydrochar derived from hydrothermal carbonization of biomass. Journal of Industrial and Engineering Chemistry 2018; **57**: 15-21

46. Gao P, Zhou Y, Meng F, Zhang Y, Liu Z, et al. Preparation and characterization of hydrochar from waste eucalyptus bark by hydrothermal carbonization. Energy 2016; **97**: 238-245

47. Krylova A Y, Zaitchenko V. Hydrothermal carbonization of biomass: a review. Solid Fuel Chemistry 2018; **52**(2): 91-103

48. Peterson A A, Vogel F, Lachance R P, Fröling M, Antal Jr M J, et al. Thermochemical biofuel production in hydrothermal media: a review of sub-and supercritical water technologies. Energy & Environmental Science 2008; **1**(1): 32-65

49. Reza M T, Upgrading biomass by hydrothermal and chemical conditioning. 2013, University of Nevada, Reno.

50. Reza M T, Andert J, Wirth B, Busch D, Pielert J, et al. Hydrothermal carbonization of biomass for energy and crop production. Applied Bioenergy 2014; **1**(1): 11-29

51. Yang W, Shimanouchi T, Wu S, Kimura Y. Investigation of the degradation kinetic parameters and structure changes of microcrystalline cellulose in subcritical water. Energy & fuels 2014; **28**(11): 6974-6980

52. Jaruwat D, Udomsap P, Chollacoop N, Fuji M, Eiad-ua A. Effects of hydrothermal temperature and time of hydrochar from Cattail leaves. in AIP Conference Proceedings. 2018. AIP Publishing LLC

53. Ali I, Naqvi S R, Bahadar A. Kinetic analysis of Botryococcus braunii pyrolysis using model-free and model fitting methods. Fuel 2018; **214**: 369-380

54. Cai J, Xu D, Dong Z, Yu X, Yang Y, et al. Processing thermogravimetric analysis data for isoconversional kinetic analysis of lignocellulosic biomass pyrolysis: Case study of corn stalk. Renewable and Sustainable Energy Reviews 2018; **82**: 2705-2715

55. Danso-Boateng E, Holdich R, Shama G, Wheatley A D, Sohail M, et al. Kinetics of faecal biomass hydrothermal carbonisation for hydrochar production. Applied energy 2013; **111**: 351-357

56. Chen R, Lu S, Zhang Y, Lo S. Pyrolysis study of waste cable hose with thermogravimetry/Fourier transform infrared/mass spectrometry analysis. Energy Conversion and Management 2017; **153**: 83-92

57. Pan L, Jiang Y, Wang L, Xu W. Kinetic study on the pyrolysis of medium density fiberboard: Effects of secondary charring reactions. Energies 2018; **11**(9): 2481

58. Álvarez-Murillo A, Sabio E, Ledesma B, Román S, González-García C. Generation of biofuel from hydrothermal carbonization of cellulose. Kinetics modelling. Energy 2016; **94**: 600-608

59. Mui E L, Cheung W, Lee V K, McKay G. Kinetic study on bamboo pyrolysis. Industrial & engineering chemistry research 2008; **47**(15): 5710-5722

Graphical abstract